

# Spin-layer locking of interlayer valley excitons trapped in moiré potentials

Mauro Brotons-Gisbert,<sup>1,\*</sup> Hyeonjun Baek,<sup>1,\*</sup> Alejandro Molina-Sánchez,<sup>2,3</sup> Dale Scerri,<sup>1</sup> Daniel White,<sup>1</sup> Kenji Watanabe,<sup>4</sup> Takashi Taniguchi,<sup>4</sup> Cristian Bonato,<sup>1</sup> and Brian D. Gerardot<sup>1,†</sup>

<sup>1</sup>*Institute of Photonics and Quantum Sciences, SUPA, Heriot-Watt University, Edinburgh EH14 4AS, UK*

<sup>2</sup>*Institute of Materials Science (ICMUV), University of Valencia, Catedrático Beltrán 2, E-46980 Valencia, Spain*

<sup>3</sup>*International Iberian Nanotechnology Laboratory (INL), Avda. Mestre José Veiga s/n, 4715-330 Braga, Portugal*

<sup>4</sup>*National Institute for Materials Science, Tsukuba, Japan*

(Dated: April 6, 2022)

Van der Waals heterostructures present unique opportunities to synthesise quantum materials. For example, atomically-thin transition metal dichalcogenides (TMDs) possess three quantum degrees of freedom: real spin, valley pseudospin, and layer pseudospin. TMD heterobilayers, in which electrons and holes reside in separate layers to form long-lived interlayer excitons (IX), offer superlative access to these features. Further, the relative stacking angle of TMD heterobilayers creates a moiré superlattice which modulates the electronic band structure in a tunable yet precise way, leading to spatial confinement of single particle wavepackets. Here we report the observation of spin-layer locking of interlayer valley excitons trapped in moiré potentials. In a heterostructure of bilayer 2H-MoSe<sub>2</sub> and monolayer WSe<sub>2</sub>, the phenomenon of locked electron spin and layer pseudospin leads to two quantum-confined IX species with distinct spin-layer-valley configurations. Furthermore, we observe the 2H-MoSe<sub>2</sub> intrinsically locks the atomic registries of the trapped IX species together. These results identify the layer pseudospin as a useful degree of freedom to engineer highly-tunable few-level quantum systems in two-dimensional heterostructures.

The electronic and optical properties of van der Waals heterostructures can be widely engineered by the diverse choice of crystal combinations [1] and their relative rotation [2–6] and interlayer spacing [7, 8]. For nearly commensurate bilayers (BLs), a slight lattice mismatch or relative rotation results in a long-range moiré superlattice which spatially modulates the electronic band-structure. Single particle wavepackets can be trapped in the periodic potential pockets with three-fold symmetry to form an intrinsic quantum dot lattice [9–11]. Recently, signatures of IX trapped in such moiré potentials were observed in TMD hetero-BL samples [12, 13].

Due to the potential to harness the real spin, valley pseudospin, and layer pseudospin [14], layered TMDs present an intriguing platform for quantum electronics and optics. The broken inversion symmetry in TMDs leads to an effective coupling between a real spin and the valley pseudospin of the electrons or holes at the  $\pm\text{K}$  corners of the hexagonal Brillouin zone [15], as shown for monolayer (ML) WSe<sub>2</sub> in Fig. 1b. Like the real spin, the valley pseudospin is associated to a magnetic moment [14, 15], which results in valley dependent selection rules. Light with  $\sigma^\pm$ -polarisation creates electron-hole pairs exclusively in the  $\pm\text{K}$  valley, enabling optical and magnetic manipulation of intralayer valley excitons [16–19]. Layer pseudospin is found in 2H-type BL TMDs which have a 180° in-plane rotation between the top- and bottom-layer and minimal interlayer electronic hopping at the K valleys [15, 20–22]. The in-plane rotation inverts the valley alignment in the two layers, such that a unique spin-valley configuration is locked to each layer, as shown for BL MoSe<sub>2</sub> in Fig. 1b. This gives rise to the

layer pseudospin. Additionally, the atomic registries of the two layers are intrinsically locked together in 2H-type BL TMDs.

Owing to these quantum degrees of freedom, TMDs are ideal ingredients to realise the concept of exciton trapping in moiré potentials [9–13]. Two different ML TMDs can be combined with an atomically sharp interface to create a hetero-BL system with Type II-band alignment [23, 24], which favours spatial separation of photogenerated carriers: electrons (holes) rapidly transfer to reside in the layer with the lowest energy conduction (valence) band-edge [25]. Due to strong Coulomb interaction, the electrons and holes form spatially-indirect interlayer excitons which exhibit the valley-dependent optical selection rules of the monolayer TMDs but with longer exciton lifetimes, robust spin-valley polarisation, and large electric field tunability [26–30]. Hetero-BLs with arbitrary stacking angles can be fabricated by transfer of mechanically exfoliated flakes [12, 13, 24, 27, 30] or chemical vapour deposition [3, 23, 25, 29]. Nearly aligned 0° (*R*-type) or 60° (*H*-type) stacking of the hetero-BL yields minimum displacement in momentum space for carriers at the band edges ( $\pm\text{K}$ ), maximizing coupling to the light cone for optical transitions [26]. As shown in Fig. 1c, IXs in an *R*-type stacked hetero-BL ( $\text{IX}^R$ ) have valley conserving ground state optical transitions, identical to monolayer TMDs. Conversely, IXs in *H*-type stacked materials ( $\text{IX}^H$ ) have valley contrasting optical transitions. We label the band-edge states at  $\pm\text{K}$  as  $|V, \uparrow / \downarrow\rangle$ ,  $|L, \uparrow / \downarrow\rangle$ , and  $|U, \uparrow / \downarrow\rangle$ , where *V* represents the WSe<sub>2</sub> valence band, *U* (*L*) is the upper (lower) MoSe<sub>2</sub> layer (layer pseudospin), and  $\uparrow$  ( $\downarrow$ ) represents the electron spin

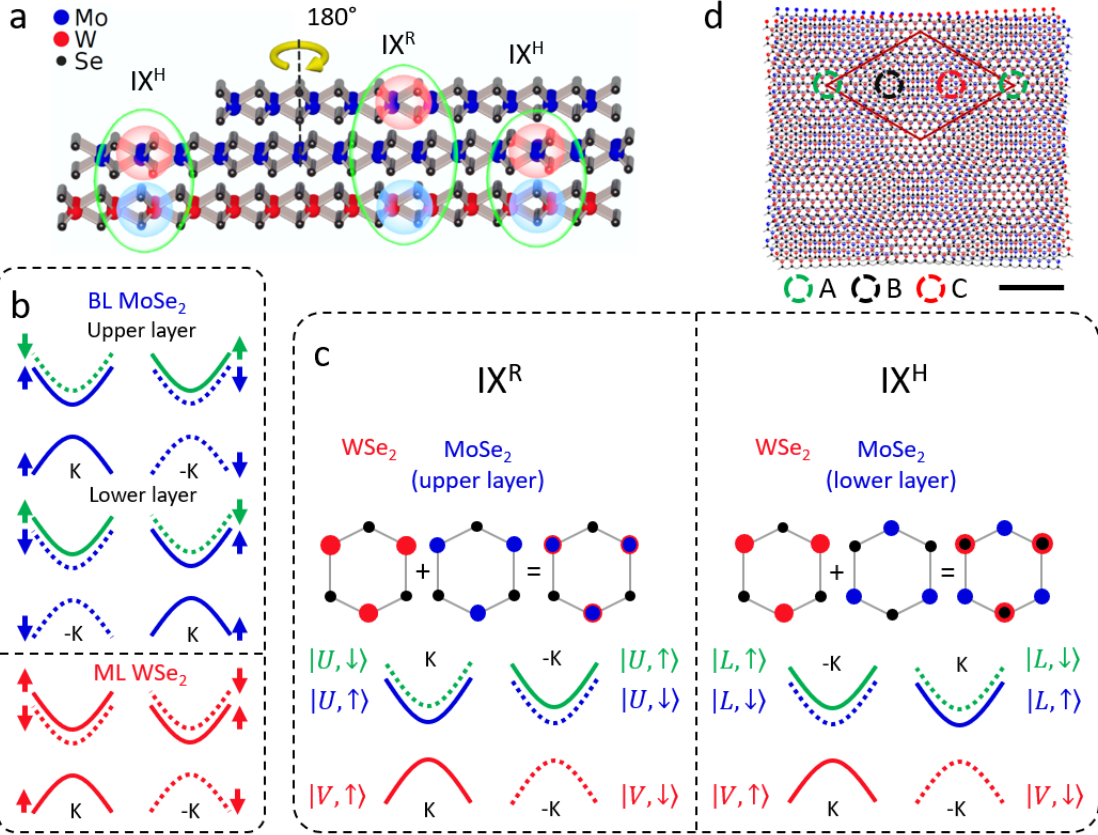


**FIG. 1: Spin-layer locking of moiré-trapped IXs in a van der Waals heterostructure.** **a**, Sketch of the heterostructures used in this work: a 2H-MoSe<sub>2</sub> crystal with ML- and BL-thick terraces stacked on top of a WSe<sub>2</sub> ML. The relative twists between the WSe<sub>2</sub> and the top and bottom MoSe<sub>2</sub> layers are  $\sim 0^\circ$  (3R stacking) and  $\sim 60^\circ$  (2H stacking), respectively. Electrons at the  $\pm K$ -valleys, localised either in the bottom or top layer MoSe<sub>2</sub>, are strongly bound to holes in the WSe<sub>2</sub>, creating two species of IX: IX<sup>H</sup> and IX<sup>R</sup>, respectively. **b**, Spin-valley locked configuration of BL 2H-MoSe<sub>2</sub> (top panel) and ML WSe<sub>2</sub> (bottom panel) at the  $\pm K$  corners of the hexagonal Brillouin zone. The red lines represent the electronic band structure at the direct band-gap edges of WSe<sub>2</sub>. The blue lines denote the valence and conduction band-edges of MoSe<sub>2</sub>, while the green lines represent the MoSe<sub>2</sub> CB excited state arising from spin-orbit coupling. The solid (dotted) lines depict spin-up (down) band-edge states. Up (down) arrows indicate spin-up (down) conduction- and valence-band electrons. **c**, Valley- and spin-layer pairing of the electrons for IX<sup>R</sup> (left) and IX<sup>H</sup> (right) together with the top views of the corresponding stacking configurations. **d**, Cartoon of the moiré superlattice formed in a R-stacked WSe<sub>2</sub>/MoSe<sub>2</sub> heterostructure with a twist angle  $\theta$  of  $5^\circ$ . Scale bar, 2 nm. The red diamond represents a moiré supercell. The three highlighted regions represent moiré-trapping sites with different local atomic configurations: A ( $R_h^h$ ), B ( $R_h^X$ ) and C ( $R_h^M$ ).

$s_z = 1/2$  ( $-1/2$ ). In addition, nearly aligned  $0^\circ$  or  $60^\circ$  stacking yields a large period moiré potential landscape in a hetero-BL in which three trapping sites (A, B, and C) with atomic registries  $R_h^h$  (A),  $R_h^X$  (B) and  $R_h^M$  (C) emerge (see Fig. 1d), where  $R_h^\mu$  denotes an R-type stacking with the  $\mu$  site of the electron layer (either  $h$  the hexagon centre,  $X$  the chalcogen site or  $M$  the metal site) vertically aligned with the hexagon centre ( $h$ ) of the hole layer [7, 9, 11].

Here we explore the spin, valley pseudospin, and layer pseudospin properties of moiré trapped IXs in an artificial trilayer (TL) heterostructure consisting of a ML WSe<sub>2</sub> and BL 2H-MoSe<sub>2</sub> (see Fig. 1a). We exploit the spin-layer locking phenomenon of BL 2H-MoSe<sub>2</sub> to

probe two moiré-trapped IX species with contrasting spin-valley alignment: the holes, localised in the WSe<sub>2</sub> layer, are strongly Coulomb bound to electrons localised in either the lower or upper MoSe<sub>2</sub> layer to form IX<sup>H</sup> or IX<sup>R</sup> species, respectively. Each localised IX species has a distinct spin-layer-valley configuration: IX<sup>R</sup> (IX<sup>H</sup>) exhibit electron-hole pairs with parallel (antiparallel) spin-valley-locked magnetic moments. The emission from each IX species exhibits circular polarisation which, when combined with knowledge of the spin and valley configuration, enable determination of the atomic registry of the moiré trapping sites. We conclude the 2H-MoSe<sub>2</sub> stacking intrinsically locks the atomic registries of IX<sup>R</sup> and IX<sup>H</sup> together.

## AB INITIO CALCULATIONS OF THE TRILAYER HETEROSTRUCTURE

To justify our choice of TL heterostructure for the realisation of spin-layer locked IXs, we performed *ab initio* calculations (see details in Methods). Figure 2 shows the calculated spin-projected band structure around the K-point. The insets show the lateral view of the calculated spatial distributions of the wave functions for electrons (top two panels) and holes (bottom panel) over the three layers. The spatial distribution of the wave functions demonstrates the type-II band alignment of the heterostructure, with the valence band state localised in the WSe<sub>2</sub> layer and the conduction band states localised in the MoSe<sub>2</sub> layers. In addition, the calculations reveal that the energy-degenerate spin-orbit-split conduction bands of BL MoSe<sub>2</sub> at K split into four different bands in the TL heterostructure (see Suppl. Fig. 2). The splitting arises from the breaking of symmetry induced by the presence of ML WSe<sub>2</sub> (see Suppl. Figs. 2-4 in Suppl. Note 2). More importantly, the calculations reveal that the four split conduction band states at K inherit the spin-layer locking of BL MoSe<sub>2</sub>, such that a unique spin and layer pseudospin can be associated to each conduction band state. In increasing energy order, the conduction band states at K can be unequivocally labelled as |L,↓⟩, |U,↑⟩, |L,↑⟩, and |U,↓⟩. Optical transitions between these conduction band states and the top valence band state at K (|V,↑⟩) give rise to four possible IX configurations: IX<sup>Hs</sup> (|V,↑⟩ ↔ |L,↑⟩), IX<sup>Ht</sup> (|V,↑⟩ ↔ |L,↓⟩), IX<sup>Rs</sup> (|V,↑⟩ ↔ |U,↑⟩), and IX<sup>Rt</sup> (|V,↑⟩ ↔ |U,↓⟩), where *s* and *t* superscripts denote spin-conserving (spin-singlet) and spin-flip (spin-triplet) optical transitions, respectively. We note that the in-plane moiré superlattice potentials are not taken into account in these calculations.

## OPTICAL SPECTROSCOPY

The artificial TL heterostructures consisted of a 2*H*-MoSe<sub>2</sub> crystal with ML and BL terraces mechanically stacked on top of a WSe<sub>2</sub> ML and encapsulated by hBN in an inert environment (see Suppl. Note 1). During the stacking process, the crystallographic axes of the ML WSe<sub>2</sub> and the BL MoSe<sub>2</sub> region were optically aligned to  $60 \pm 3^\circ$ . Figure 3a shows representative low-temperature ( $T = 4$  K) confocal photoluminescence (PL) spectra measured using continuous wave excitation at 2.33 eV and an excitation power ( $P_{exc}$ ) of 4  $\mu$ W. PL spectra corresponding to different positions of the ML MoSe<sub>2</sub>/ML WSe<sub>2</sub> heterostructure (black and blue spectra) show emission in the energy range 1.32 - 1.42 eV (energy range I). We observe that the emission is centred around two main energy windows (1.385 - 1.405 eV and 1.345 - 1.375 eV), but with spatially dependent relative intensities. Positions A

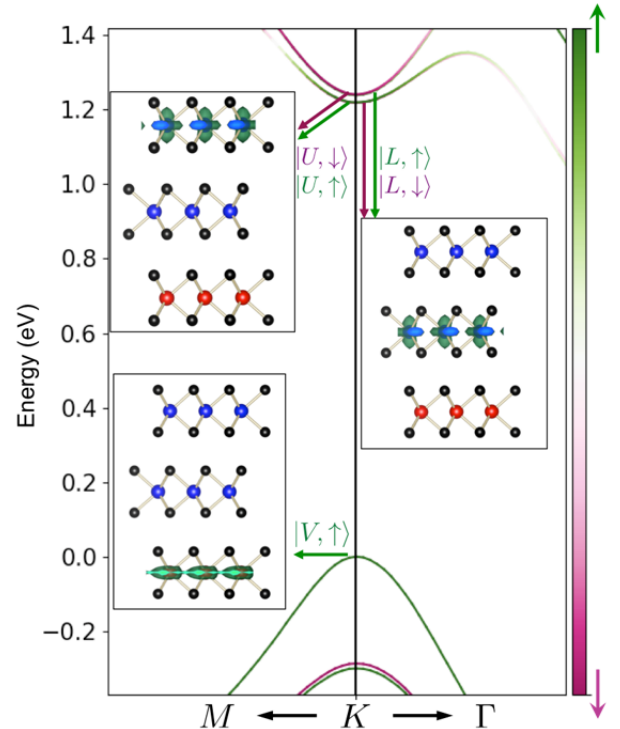
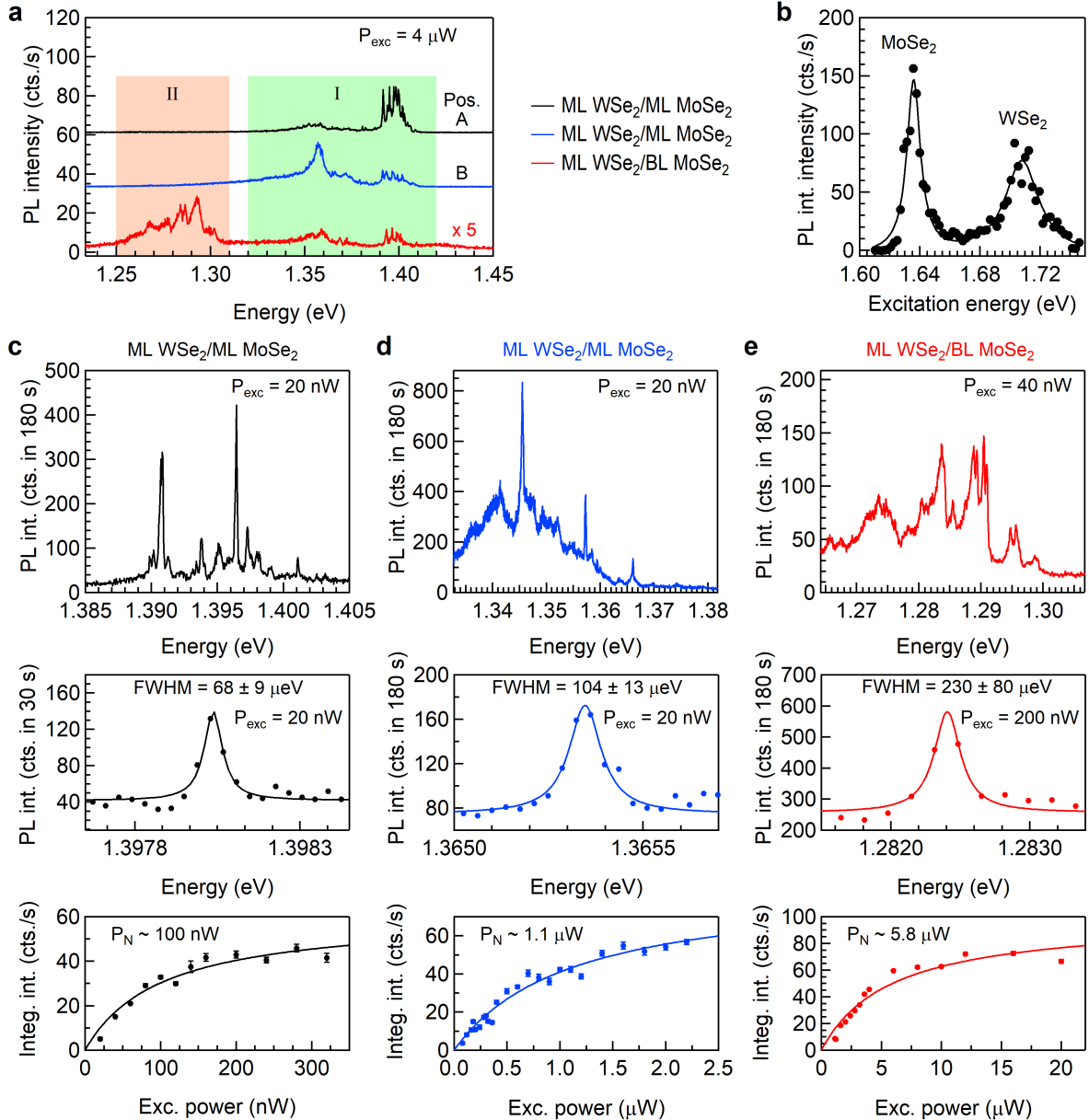


FIG. 2: Spin-projected band structure of the TL around the *K* point with the wave functions corresponding to the top of the valence band (|V,↑⟩) and bottom of the conduction band (|L,↓⟩, |U,↑⟩, |L,↑⟩, and |U,↓⟩, in increasing energy order). A more detailed description of the conduction band states is shown in the Suppl. Fig. 2.

(black spectrum) and B (blue spectrum) correspond to the spatial positions with the brightest relative intensities for the two windows. To confirm that the observed emission arises from IXs, we performed PL excitation spectroscopy, scanning a continuous-wave excitation laser from 1.61 eV to 1.75 eV while monitoring the intensity of the emission peaks. Figure 3b shows a representative PL excitation spectrum, featuring two prominent resonances which correspond to the absorption of the intralayer 1s exciton states in ML MoSe<sub>2</sub> and WSe<sub>2</sub>. PL spectra in the TL part of the heterostructure is markedly different: emission in spectral region I is still observed but with reduced intensity relative to a new band of emission at lower energy (1.25 - 1.31 eV, region II), see for example the red spectrum in Fig. 3a. The spatial dependence of the PL spectra suggests that ranges I and II originate from different IX species, as expected from the stacking configuration presented in Fig. 1. Therefore, we label IXs with emission in ranges I and II as IX<sup>H</sup> and IX<sup>R</sup>, respectively. The PL emission energy of IX<sup>H</sup> matches well with recent reports for IX emission in MoSe<sub>2</sub>/WSe<sub>2</sub> hetero-BLs [12, 27, 29–31], while IX<sup>R</sup> emission in TL heterostructures have yet to be explored in such detail.

With reducing  $P_{exc}$ , the broad PL gradually disappears



**FIG. 3: Optical spectroscopy properties of spin-layer-locked IXs trapped in moiré potentials.** **a**, Low-temperature confocal PL spectra measured at three spatial positions of the heterostructure. The black and blue positions (A and B, respectively) represent spectra corresponding to different positions of the ML MoSe<sub>2</sub>/ML WSe<sub>2</sub> heterostructure, with emission in energy range I (1.32 - 1.42 eV). The red line corresponds to a spectrum measured in the ML WSe<sub>2</sub>/BL MoSe<sub>2</sub> region of the heterostructure, with emission in energy range II (1.25 - 1.31 eV). **b**, Photoluminescence excitation intensity plot of a representative IX, showing two resonances corresponding to the intralayer exciton states in ML MoSe<sub>2</sub> and ML WSe<sub>2</sub>. **c-e**, Optical spectra (top panels), single peak linewidths (middle panels), and power dependence of the single peaks (bottom panels) of representative IXs trapped in moiré potentials in the ML WSe<sub>2</sub>/ML MoSe<sub>2</sub> (**c** and **d**), and the ML WSe<sub>2</sub>/BL MoSe<sub>2</sub> regions of the heterostructure (**e**).

until the sharp peaks dominate, as shown in the top panels of Figs. 3c-3e. Here, high-resolution PL spectra are measured at the spatial positions corresponding to the spectra shown in Fig. 3a but with reduced  $P_{exc}$ . The IX<sup>H</sup> (IX<sup>R</sup>) PL peaks exhibit Lorentzian lineshapes with average full-width at half maximum (FWHM) of  $\sim 100$

$\mu\text{eV}$  ( $\sim 250 \mu\text{eV}$ ); the narrowest peaks observed are  $\sim 70 \mu\text{eV}$ , as shown in the middle panel of Fig. 3c. These linewidths, two orders of magnitude narrower than typical IX linewidths in WSe<sub>2</sub>/MoSe<sub>2</sub> hetero-BLs [28–30, 32], are comparable to quantum emitters in ML WSe<sub>2</sub> [33–35] and to recently reported moiré-trapped excitons [12].

Supplementary Figure 5 shows the full evolution of the  $\text{IX}^H$  emission under increasing  $P_{exc}$ . Additionally, we observe minimal spectral wandering ( $< 10 \mu\text{eV}$ ) at long time scales (see Suppl. Fig. 6). For each species of IX, the intensity saturates with increasing  $P_{exc}$  (bottom row of Figs. 3c-e). The power dependence of the intensity is described by a two-level saturation model:  $I = I_{sat}(P_{exc}/(P_{exc} + P_N))$ , where  $P_N$  is the normalised excitation power at which integrated intensity ( $I$ ) of the PL peak becomes half of the saturation integrated intensity ( $I_{sat}$ ). We find  $P_N$  of individual emitters varies substantially for different spatial positions.

### SPIN-VALLEY-LAYER CONFIGURATIONS OF $\text{IX}^R$ AND $\text{IX}^H$

The narrow linewidths and saturation behaviour provide strong evidence of IXs trapped in a moiré confinement potential. To confirm these peaks arise from band-edge states and disentangle the spin-layer-valley configuration of each exciton species, we perform magneto-optical spectroscopy measurements in Faraday configuration. Figure 4a shows the magnetic field ( $B_z$ ) dependence of representative moiré-trapped  $\text{IX}^R$  and  $\text{IX}^H$  (left and right panel, respectively). A clear linear Zeeman splitting with increasing  $B_z$  is observed for every peak, and it is immediately noticeable that the  $g$ -factor of  $\text{IX}^H$  excitons is considerably larger than  $\text{IX}^R$  excitons. To confirm these are universal features of moiré trapped  $\text{IX}^H$  and  $\text{IX}^R$ , a second WSe<sub>2</sub>/MoSe<sub>2</sub> heterostructure with both ML WSe<sub>2</sub>/ML MoSe<sub>2</sub> and ML WSe<sub>2</sub>/BL MoSe<sub>2</sub> regions and similar stacking angle ( $\sim 60^\circ$  between the ML WSe<sub>2</sub>/BL MoSe<sub>2</sub>) was fabricated and measured (Sample 2). Sample 2 also exhibits  $\text{IX}^R$  and  $\text{IX}^H$  with narrow emission peaks in the same energy ranges as Sample 1. Figure 4b summarises the measured  $g$ -values for each IX species in Samples 1 and 2 (black and red dots, respectively) as a function of their emission energy. Trapped  $\text{IX}^R$ , which only appear in energy range II from the TL part of the samples, exhibit a  $g$ -factor of  $-7.0 \pm 0.6$ . On the other hand, trapped  $\text{IX}^H$  in energy range I are observed both in the hetero-BL and hetero-TL regions and exhibit a  $g$ -factor of  $-15.76 \pm 0.13$ .

The striking  $B_z$  dependence for each IX species has its origin in their corresponding spin-valley configuration [12] (see top panel of Fig. 4c), demonstrating that  $\text{IX}^R$  and  $\text{IX}^H$  preserve the spin-layer locking of BL 2H-MoSe<sub>2</sub>. Since both carrier spin and valley pseudospin are associated to a magnetic moment [14, 15], the total valley-selective splitting of the interlayer transitions ( $\Delta$ ) amounts to [12, 36]

$$\Delta(B_z) = E^{\sigma^+}(B_z) - E^{\sigma^-}(B_z) = g\mu_B B_z, \quad (1)$$

with  $g$  being an effective  $g$ -factor,  $\mu_B$  being the Bohr magneton, and  $E^{\sigma^\pm}(B_z)$  being the  $B_z$ -dependent ener-

gies of the intervalley transitions with  $\sigma^\pm$  polarisation.  $E^{\sigma^\pm}$  is defined as the energy difference between the conduction ( $E_c^\pm$ ) and valence ( $E_v^\pm$ ) band edges associated to  $\sigma^\pm$  transitions ( $E^{\sigma^\pm}(B_z) = E_c^\pm - E_v^\pm$ ). The Zeeman shift of the  $E_c^\pm$  ( $\Delta E_c$ ) and  $E_v^\pm$  ( $\Delta E_v$ ) band edges can be estimated as a combination of three different magnetic moment contributions:  $\Delta E_{c/v} = \Delta_s + \Delta_a + \Delta_v$ , where  $\Delta_s = 2s_z\mu_B B_z$  is the spin contribution,  $\Delta_a = l_{c/v}\mu_B B_z$  is the atomic orbital contribution, and  $\Delta_v = \tau\alpha_{c/v}\mu_B B_z$  represents the valley contribution arising from the Berry curvature [15]. Here,  $s_z = \pm 1/2$  is the electron spin,  $l_c = 0$  ( $l_v = 2\tau$ ) is the magnetic quantum number for the atomic orbital at the conduction (valence) band edge,  $\tau = \pm 1$  is the index for the  $\pm K$  valleys, and  $\alpha_c$  ( $\alpha_v$ ) is the magnetic moment of the conduction (valence) band edge [18]. According to the leading order of a simplified  $\mathbf{k}\cdot\mathbf{p}$  approximation for the band-edge carriers [15, 37], the valley magnetic moments of the conduction and valence band can be estimated as  $\alpha_{c,v} = m_0/m_{e,h}^*$ , with  $m_0$  the free electron mass and  $m_e^*$  ( $m_h^*$ ) the electron (hole) effective mass at the conduction (valence) band edge. The middle panels of Fig. 4c show the Zeeman shifts of the conduction (MoSe<sub>2</sub>) and valence (WSe<sub>2</sub>) band edges of a WSe<sub>2</sub>/MoSe<sub>2</sub> heterostructure calculated using  $m_h^* = 0.37 m_0$  [38] and  $m_e^* = 0.84 m_0$  [39, 40]. Here we assume that the spin-split conduction bands at the  $\pm K$  points of ML and BL MoSe<sub>2</sub> have similar effective masses [39], and therefore we use the same  $\alpha_c$  for both. The colour and line style used for each band edge are consistent with the schematics of the spin-layer configuration shown in the top panel of the figure. Solid (dashed) lines represent the Zeeman shifts of band edges with spin up (down). Red lines represent the Zeeman shifts of the valence band states in WSe<sub>2</sub>, whereas blue and green lines represent the Zeeman shifts of the MoSe<sub>2</sub> conduction band edges with parallel and antiparallel valley and spin configuration, respectively.

According to Equation (1), the different spin-layer-valley configuration of  $\text{IX}^R$  and  $\text{IX}^H$  excitons results in different total Zeeman splittings  $\Delta$ . Therefore, the  $g$ -factor of the moiré-trapped valley excitons is representative of their spin-valley configuration, which, as a consequence of the spin-layer locking of BL MoSe<sub>2</sub>, also indicates whether the electron is localised in the bottom or top MoSe<sub>2</sub> layer. Furthermore, two different  $\Delta$  splittings are possible for both  $\text{IX}^R$  and  $\text{IX}^H$  excitons depending on the conduction bands involved in the optical transitions. Using Eq. (1),  $\text{IX}^R$  excitons can take  $\Delta$  values of:

$$|\Delta E^{Rs}(B_z)| = 2|2 + \alpha_v - \alpha_c|\mu_B B_z, \quad (2)$$

and

$$|\Delta E^{Rt}(B_z)| = 2|4 + \alpha_v - \alpha_c|\mu_B B_z; \quad (3)$$

while  $\text{IX}^H$  excitons can present  $\Delta$  values of:

$$|\Delta E^{Hs}(B_z)| = 2|2 + \alpha_v + \alpha_c|\mu_B B_z, \quad (4)$$

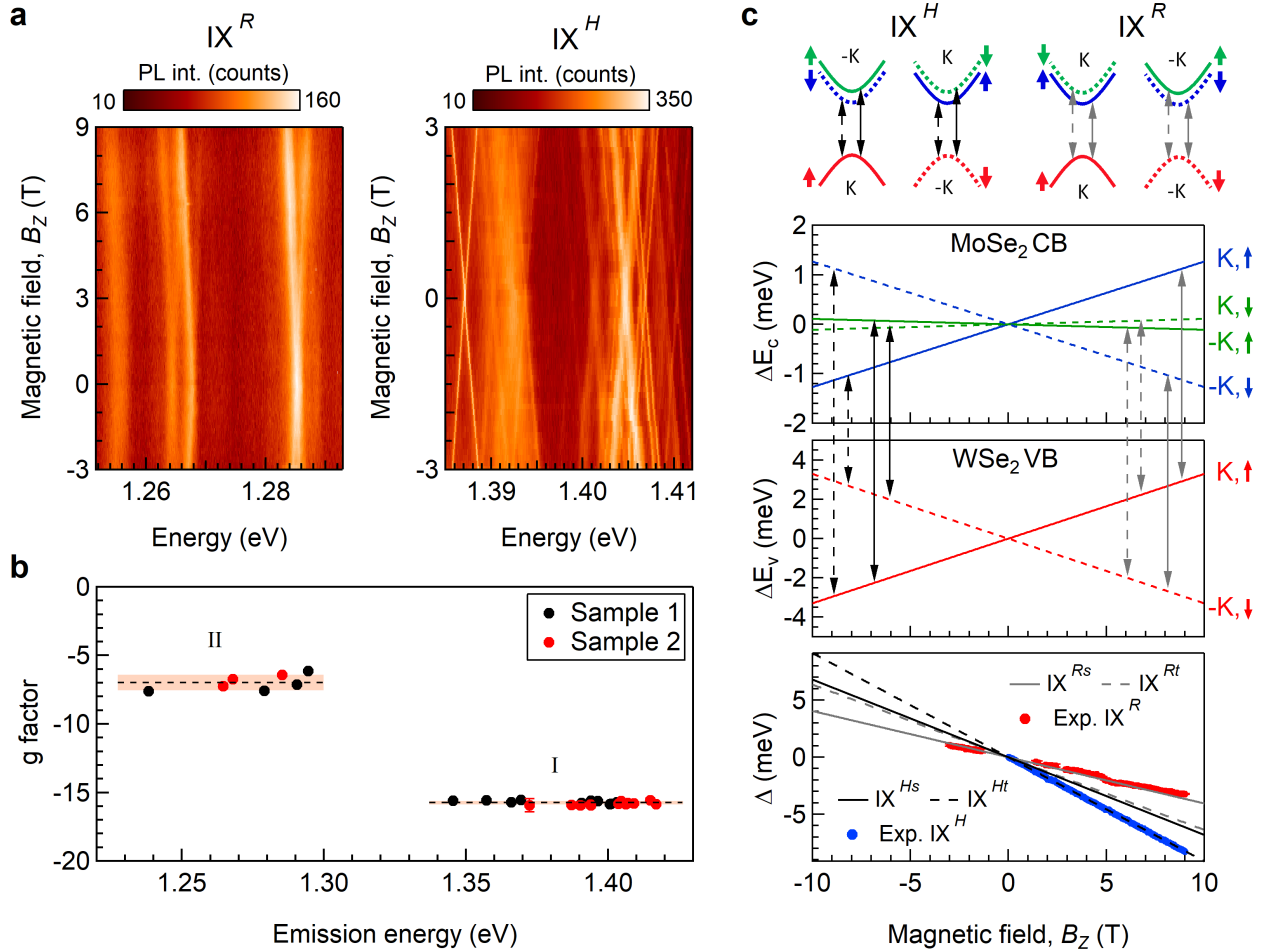


**FIG. 4: Magneto-optic properties of spin-layer-locked IXs trapped in moiré potentials.** **a**, Magnetic field dependence of representative moiré-trapped  $\text{IX}^R$  (left) and  $\text{IX}^H$  excitons (right) as a function of an applied out-of-plane magnetic field. **b**, Summary of the  $g$ -factor values measured for moiré-trapped  $\text{IX}^R$  and  $\text{IX}^H$  excitons in heterostructures 1 (black dots) and 2 (red dots) as a function of their emission energies. **c**, Top panel: schematics of the spin-valley configuration for  $\text{IX}^R$  (left) and  $\text{IX}^H$  (right) excitons. Middle panels: Zeeman shifts for the conduction (MoSe<sub>2</sub>) and valence (WSe<sub>2</sub>) band edges calculated by using Eqs. (2)-(5). The vertical arrows represent the optical transitions for each IX exciton and spin configuration. Grey (black) arrows represent optical transitions in  $\text{IX}^R$  ( $\text{IX}^H$ ) excitons, while solid (dashed) lines represent spin-singlet (spin-triplet) optical transitions. Bottom panel:  $B_z$ -dependence of the  $\Delta$  value for each IX exciton species and spin configuration as calculated from Eqs. (2)-(5). The colour and line style used for the  $\Delta$  value of each IX configuration is consistent with the optical transitions of the corresponding excitons in the middle panels. Red and blue dots represent the  $B_z$ -dependence of the experimental  $\Delta$  values of representative trapped  $\text{IX}^R$  and  $\text{IX}^H$  excitons, respectively, as extracted from Lorentzian fits of the experimental data. Here the error bar size is smaller than the data points

and

$$|\Delta E^{Ht}(B_z)| = 2|4 + \alpha_v + \alpha_c| \mu_B B_z. \quad (5)$$

The vertical arrows in the middle panels of Fig. 4c represent the optical transitions responsible of the Zeeman splittings for each IX exciton and spin configuration. Grey (black) arrows represent optical transitions in  $\text{IX}^R$  ( $\text{IX}^H$ ) excitons, while solid (dashed) lines represent spin-singlet (spin-triplet) optical transitions. The bottom panel of Fig. 4c shows the  $B_z$ -dependence of the  $\Delta$  value for each IX exciton and spin configuration as calcu-

lated from Equations (2)-(5). The colour and line style used for the  $\Delta$  value of each IX configuration is consistent with the one employed to indicate the optical transitions of the corresponding excitons. The bottom panel of Fig. 4c also shows the  $B_z$ -dependence of the experimental  $\Delta$  values of two representative trapped  $\text{IX}^R$  (red dots) and  $\text{IX}^H$  (blue dots) excitons, as extracted from Lorentzian fits of the experimental data. The good agreement observed between the calculated and experimental  $\Delta$  values corroborates our initial identification of  $\text{IX}^R$  and  $\text{IX}^H$  excitons. Based on Equations (2)-(5) and the

stacking configuration of the heterostructures studied in this work (see Fig. 1a), IXs with larger absolute values of the  $g$ -factor ( $\text{IX}^H$ ) should be observed in both the hetero-BL and TL regions of the heterostructures, whereas IXs with smaller absolute values of the  $g$ -factor ( $\text{IX}^R$ ) should be exclusively present in the TL regions. Moreover, the magneto-optical measurements provide additional information. The results shown in Fig. 4c indicate that the observed  $\text{IX}^R$  and  $\text{IX}^H$  excitons arise from optical transitions involving the lowest spin-split conduction band of  $\text{MoSe}_2$  at  $\pm K$ . This observation leads to spin-conserved and spin-flip optical transitions for  $\text{IX}^R$  and  $\text{IX}^H$  excitons, respectively. Although the latter is normally forbidden in ML TMDs due to its spin-flip nature, it can be brightened due to the selection rules dictated by the resulting interlayer atomic registry of the moiré pattern in our heterostructures [11].

The spin-layer-locking induced coexistence of  $\text{IX}^R$  and  $\text{IX}^H$  in the TL heterostructure allows us to estimate the magnetic moment contribution of the conduction and valence band edges. From the combination of Equations (2) and (5), and the measured  $g$ -factors for  $\text{IX}^H$  and  $\text{IX}^R$ , we estimate valley  $g$ -factors of  $\alpha_v = 2.69 \pm 0.15$  and  $\alpha_c = 1.19 \pm 0.15$ . The estimated valley  $g$ -factors yield effective masses of  $m_e^* \approx 0.84 \pm 0.11 m_0$  and  $m_h^* \approx 0.37 \pm 0.02 m_0$  for electrons and holes at the bottom conduction band of  $\text{MoSe}_2$  and top valence band of  $\text{WSe}_2$ , respectively. The estimated carrier effective masses agree well with previously calculated and experimental values [38–40].

### LOCAL ATOMIC REGISTRIES OF MOIRÉ TRAPPING SITES

The relative Zeeman shifts of the conduction and valence band edges at  $\pm K$  points enable further insight, based on the fact that the  $B_z$ -induced shift of the  $\text{WSe}_2$  valence band edge is larger than the corresponding shifts of the  $\text{MoSe}_2$  conduction bands (as shown in Fig. 4c). The smaller Zeeman splitting for the conduction band edges is a consequence of two factors: the smaller magnetic moment contribution from the atomic orbitals of the conduction band ( $l_c = 0$ ), and the higher effective mass of electrons in the conduction band of  $\text{MoSe}_2$ . The larger Zeeman shift for the valence band edges leads to a striking consequence: for  $B_z > 0$ , the energy of the optical transitions involving the valence band edges of  $\text{WSe}_2$  at  $K$  (- $K$ ) always shift to lower (higher) energies regardless of the spin-valley configuration of the IX. Based on this, helicity-resolved PL measurements can provide information about the nature of the moiré confinement potential. Figures 5a and 5b show circularly-polarised-resolved spectra of representative  $\text{IX}^H$  and  $\text{IX}^R$ , respectively, under linearly polarised ( $\pi$ ) excitation at 2.33 eV and different applied magnetic fields. Both  $\text{IX}^H$  and  $\text{IX}^R$  exhibit strong circular polarisation, and application of

$B_z$  results in a Zeeman shift of the  $\sigma^+$ -polarised ( $\sigma^-$ -polarised) PL peak towards lower (higher) energies. For zero magnetic field, energy-degenerate  $\sigma^+$  and  $\sigma^-$  emissions are observed with near identical intensity, indicating that the IXs are trapped in confinement potentials that preserve the rotational  $C_3$  symmetry. The degenerate circularly-polarised emission of  $\text{IX}^R$  and  $\text{IX}^H$  contrasts with the emission polarisation properties of neutral excitons in quantum emitters in ML  $\text{WSe}_2$ , which typically exhibit a large fine-structure splitting and strictly linear polarisation [33–35] arising from the electron-hole exchange interaction energy and asymmetry in the confinement potential. The absence of observable fine-structure splitting is only expected in cases for which rotational symmetry of the crystal lattice and confining potential is maintained.

The polarisation selection rules of the moiré-trapped excitons are dictated by the local atomic registry of the moiré trapping site [9, 11]. Figure 5c shows the selection rules for optical transitions involving the  $K$ -point valence band for both spin-singlet and spin-triplet IXs trapped in moiré potential sites with different atomic registries [11]. Accordingly, the results in Figs. 5a and 5b indicate that  $\text{IX}^R$  and  $\text{IX}^H$  originate from IXs trapped in moiré potentials with interlayer atomic registries  $R_h^h$  (A) and  $H_h^h$  (B), respectively. Interestingly, we find that  $\text{IX}^R$  excitons in the TL heterostructure present different polarisation selection rules than IXs in 3R-type stacked  $\text{WSe}_2/\text{MoSe}_2$  hetero-BLs [12]. We attribute the different behaviour to the 2H-type stacking of BL  $\text{MoSe}_2$ , which intrinsically locks the atomic registries of  $\text{IX}^R$  and  $\text{IX}^H$  together (see left panel of Fig. 5c).

### DISCUSSION AND OUTLOOK

The magneto-optical spectroscopy experiments reveal the remarkable consequence of spin-layer locking of moiré-trapped excitons in the artificial TL heterostructures. Two IX species,  $\text{IX}^R$  and  $\text{IX}^H$ , with distinct spin-valley-layer configurations are observed:  $\text{IX}^R$  ( $\text{IX}^H$ ) composed of electrons in the top (bottom)  $\text{MoSe}_2$  layer present carriers with parallel (antiparallel) spin-valley locked contributions, resulting in an effective layer-locking of the Landé  $g$ -factors of the trapped IX. At cryogenic temperatures, both trapped IX species exhibit narrow linewidths and saturate with increasing excitation power, hallmarks of a few-level quantum confined system. An unambiguous demonstration of quantum emission from the moiré-trapped excitons, for instance photon antibunching, remains an important target. Finally, by applying the selection rules for trapped IX with rotational  $C_3$  symmetry, polarisation dependent spectroscopy identifies that the 2H-type stacking of BL  $\text{MoSe}_2$  intrinsically locks the atomic registries of the two IX together.

For quantum information applications, a basic require-

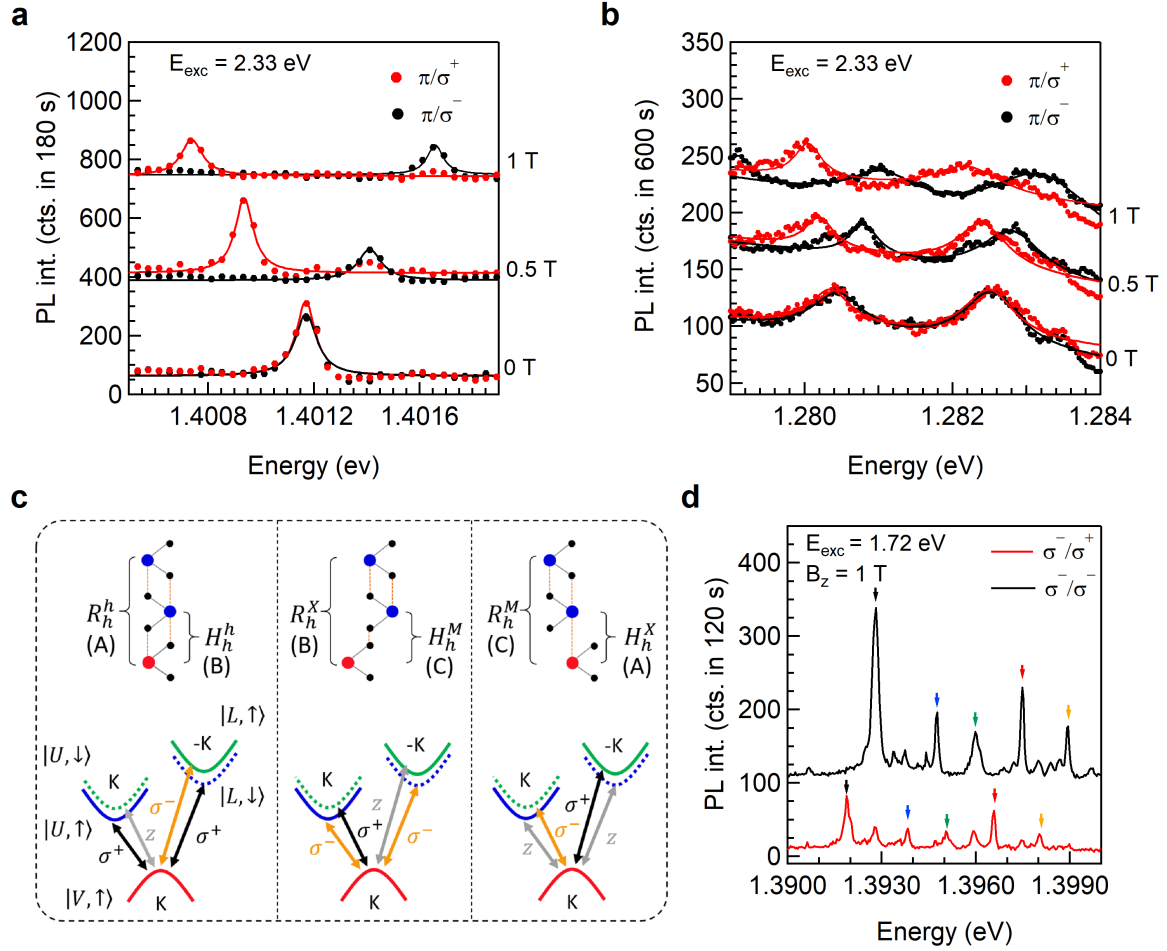


FIG. 5: **Optical selection rules of spin-layer-locked IXs trapped in moiré potentials.** **a-b**, Circularly-polarised-resolved PL spectra of representative  $IX^H$  and  $IX^R$  excitons, respectively, under linearly polarised excitation at 2.33 eV and different applied magnetic fields. **c**, Schematics of the selection rules for optical transitions involving the K-point valence band for both spin-singlet and spin-triplet IXs trapped in moiré potential sites with different atomic registries [11]. Black, orange and grey double arrows represent optical transitions with  $\sigma^+$ ,  $\sigma^-$ , and  $z$  polarisation. **d**, Circularly-polarised-resolved PL spectra of a representative  $IX^H$  trapped exciton under  $\sigma^-$  excitation resonant to the A exciton of ML WSe<sub>2</sub> with an applied magnetic field of 1 T. The coloured arrows indicate the Zeeman-split peaks belonging to the same emitters.

ment is the ability to initialise the state of the few-level quantum system, which has been achieved for valley qubits in ML TMDs via optical pumping [16, 17]. Here we show the trapped IXs retain the strong valley polarisation of the constituent ML semiconductors. Fig. 5d shows the valley polarisation of trapped  $IX^H$  under  $\sigma^-$  excitation resonant to the A exciton of ML WSe<sub>2</sub>. A degree of circular polarisation ( $P_c$ ) of  $\sim 60\%$  is estimated from these measurements. Supplementary Figure 8a shows that  $\sigma^+$  excitation resonant to the A exciton of WSe<sub>2</sub> gives rise to a similar  $P_c$ , confirming the expected time-reversal process. Conversely, no appreciable valley polarisation is observed under  $\sigma^\pm$  excitation resonant to the A exciton of ML MoSe<sub>2</sub> (see Suppl. Figs. 8b and 8c). This result is in agreement with previous observations where a  $P_C \approx 0$  was observed for resonant

excitation to the A exciton of MoSe<sub>2</sub> under  $\sigma$  excitation [30, 41].

Finally, we remark that the phenomenon of spin-layer locking provides a means to engineer few-level quantum systems in van der Waals heterostructures. For example, the selection rules arising from the  $C_3$  symmetry for the atomic registries we observe (left panel of Fig. 5d), create a “vee-type” three level system: a single ground state ( $|V, \uparrow\rangle$ ) couples to two non-degenerate excited states ( $|L, \downarrow\rangle$  and  $|U, \uparrow\rangle$ ). Alternatively, a three-level system analogous to a “spin-lambda” type atom, in which two ground states couple to a common excited state, can be engineered using the layer-pseudospin degree of freedom in a TL heterostructure consisting of BL 2H-WSe<sub>2</sub>/ML MoSe<sub>2</sub>. This quantum state engineering opens new opportunities for advanced quantum control techniques in

the van der Waals platform.

---

\* These authors contributed equally to this work;  
Electronic address: M.Brotons.i.Gisbert@hw.ac.uk;  
h.baek@hw.ac.uk

† Electronic address: B.D.Gerardot@hw.ac.uk

[1] A. K. Geim and I. V. Grigorieva, *Van der waals heterostructures*, *Nature* **499**, 419 (2013).

[2] R. Bistritzer and A. H. MacDonald, *Moiré bands in twisted double-layer graphene*, *Proceedings of the National Academy of Sciences* **108**, 12233 (2011).

[3] C. Zhang, C.-P. Chuu, X. Ren, M.-Y. Li, L.-J. Li, C. Jin, M.-Y. Chou, and C.-K. Shih, *Interlayer couplings, Moiré patterns, and 2D electronic superlattices in MoS<sub>2</sub>/WSe<sub>2</sub> heterobilayers*, *Science Advances* **3**, e1601459 (2017).

[4] Y. Cao, V. Fatemi, S. Fang, K. Watanabe, T. Taniguchi, E. Kaxiras, and P. Jarillo-Herrero, *Unconventional superconductivity in magic-angle graphene superlattices*, *Nature* **556**, 43 (2018).

[5] C. Jin, E. C. Regan, A. Yan, M. I. B. Utama, D. Wang, S. Zhao, Y. Qin, S. Yang, Z. Zheng, S. Shi, *et al.*, *Observation of moiré excitons in WSe<sub>2</sub>/WS<sub>2</sub> heterostructure superlattices*, *Nature* **567**, 76 (2019).

[6] E. M. Alexeev, D. A. Ruiz-Tijerina, M. Danovich, M. J. Hamer, D. J. Terry, P. K. Nayak, S. Ahn, S. Pak, J. Lee, J. I. Sohn, *et al.*, *Resonantly hybridized excitons in moiré superlattices in van der Waals heterostructures*, *Nature* **567**, 81 (2019).

[7] Q. Tong, H. Yu, Q. Zhu, Y. Wang, X. Xu, and W. Yao, *Topological mosaics in moiré superlattices of van der Waals heterobilayers*, *Nature Physics* **13**, 356 (2017).

[8] M. Yankowitz, J. Jung, E. Laksono, N. Leconte, B. L. Chittari, K. Watanabe, T. Taniguchi, S. Adam, D. Graf, and C. R. Dean, *Dynamic band-structure tuning of graphene moiré superlattices with pressure*, *Nature* **557**, 404 (2018).

[9] H. Yu, G.-B. Liu, J. Tang, X. Xu, and W. Yao, *Moiré excitons: From programmable quantum emitter arrays to spin-orbit-coupled artificial lattices*, *Science Advances* **3**, e1701696 (2017).

[10] F. Wu, T. Lovorn, and A. MacDonald, *Theory of optical absorption by interlayer excitons in transition metal dichalcogenide heterobilayers*, *Physical Review B* **97**, 035306 (2018).

[11] H. Yu, G.-B. Liu, and W. Yao, *Brightened spin-triplet interlayer excitons and optical selection rules in van der waals heterobilayers*, *2D Materials* **5**, 035021 (2018).

[12] K. L. Seyler, P. Rivera, H. Yu, N. P. Wilson, E. L. Ray, D. G. Mandrus, J. Yan, W. Yao, and X. Xu, *Signatures of moiré-trapped valley excitons in MoSe<sub>2</sub>/WSe<sub>2</sub> heterobilayers*, *Nature* **567**, 66 (2019).

[13] K. Tran, G. Moody, F. Wu, X. Lu, J. Choi, K. Kim, A. Rai, D. A. Sanchez, J. Quan, A. Singh, *et al.*, *Evidence for moiré excitons in van der Waals heterostructures*, *Nature* **1** (2019).

[14] X. Xu, W. Yao, D. Xiao, and T. F. Heinz, *Spin and pseudospins in layered transition metal dichalcogenides*, *Nature Physics* **10**, 343 (2014).

[15] D. Xiao, G.-B. Liu, W. Feng, X. Xu, and W. Yao, *Coupled spin and valley physics in monolayers of MoS<sub>2</sub> and other group-VI dichalcogenides*, *Physical Review Letters* **108**, 196802 (2012).

[16] K. F. Mak, K. He, J. Shan, and T. F. Heinz, *Control of valley polarization in monolayer MoS<sub>2</sub> by optical helicity*, *Nature Nanotechnology* **7**, 494 (2012).

[17] H. Zeng, J. Dai, W. Yao, D. Xiao, and X. Cui, *Valley polarization in MoS<sub>2</sub> monolayers by optical pumping*, *Nature Nanotechnology* **7**, 490 (2012).

[18] G. Aivazian, Z. Gong, A. M. Jones, R.-L. Chu, J. Yan, D. G. Mandrus, C. Zhang, D. Cobden, W. Yao, and X. Xu, *Magnetic control of valley pseudospin in monolayer WSe<sub>2</sub>*, *Nature Physics* **11**, 148 (2015).

[19] A. Srivastava, M. Sidler, A. V. Allain, D. S. Lembke, A. Kis, and A. Imamoğlu, *Valley Zeeman effect in elementary optical excitations of monolayer WSe<sub>2</sub>*, *Nature Physics* **11**, 141 (2015).

[20] Z. Gong, G.-B. Liu, H. Yu, D. Xiao, X. Cui, X. Xu, and W. Yao, *Magnetoelectric effects and valley-controlled spin quantum gates in transition metal dichalcogenide bilayers*, *Nature Communications* **4**, 2053 (2013).

[21] A. M. Jones, H. Yu, J. S. Ross, P. Klement, N. J. Ghimire, J. Yan, D. G. Mandrus, W. Yao, and X. Xu, *Spin-layer locking effects in optical orientation of exciton spin in bilayer WSe<sub>2</sub>*, *Nature Physics* **10**, 130 (2014).

[22] J. M. Riley, F. Mazzola, M. Dendzik, M. Michiardi, T. Takayama, L. Bawden, C. Granerød, M. Leandersson, T. Balasubramanian, M. Hoesch, *et al.*, *Direct observation of spin-polarized bulk bands in an inversion-symmetric semiconductor*, *Nature Physics* **10**, 835 (2014).

[23] M.-H. Chiu, C. Zhang, H.-W. Shiu, C.-P. Chuu, C.-H. Chen, C.-Y. S. Chang, C.-H. Chen, M.-Y. Chou, C.-K. Shih, and L.-J. Li, *Determination of band alignment in the single-layer MoS<sub>2</sub>/WSe<sub>2</sub> heterojunction*, *Nature Communications* **6**, 7666 (2015).

[24] N. R. Wilson, P. V. Nguyen, K. Seyler, P. Rivera, A. J. Marsden, Z. P. Laker, G. C. Constantinescu, V. Kandyba, A. Barinov, N. D. Hine, X. Xu, and D. H. Cobden, *Determination of band offsets, hybridization, and exciton binding in 2D semiconductor heterostructures*, *Science Advances* **3**, e1601832 (2017).

[25] X. Hong, J. Kim, S.-F. Shi, Y. Zhang, C. Jin, Y. Sun, S. Tongay, J. Wu, Y. Zhang, and F. Wang, *Ultrafast charge transfer in atomically thin MoS<sub>2</sub>/WS<sub>2</sub> heterostructures*, *Nature Nanotechnology* **9**, 682 (2014).

[26] H. Yu, Y. Wang, Q. Tong, X. Xu, and W. Yao, *Anomalous light cones and valley optical selection rules of interlayer excitons in twisted heterobilayers*, *Physical Review Letters* **115**, 187002 (2015).

[27] P. Rivera, J. R. Schaibley, A. M. Jones, J. S. Ross, S. Wu, G. Aivazian, P. Klement, K. Seyler, G. Clark, N. J. Ghimire, J. Yan, D. G. Mandrus, W. Yao, and X. Xu, *Observation of long-lived interlayer excitons in monolayer MoSe<sub>2</sub>-WSe<sub>2</sub> heterostructures*, *Nature Communications* **6**, 6242 (2015).

[28] P. Rivera, K. L. Seyler, H. Yu, J. R. Schaibley, J. Yan, D. G. Mandrus, W. Yao, and X. Xu, *Valley-polarized exciton dynamics in a 2D semiconductor heterostructure*, *Science* **351**, 688 (2016).

[29] A. T. Hanbicki, H.-J. Chuang, M. R. Rosenberger, C. S. Hellberg, S. V. Sivaram, K. M. McCreary, I. I. Mazin, and B. T. Jonker, *Double indirect interlayer exciton in a MoSe<sub>2</sub>/WSe<sub>2</sub> van der Waals heterostructure*, *Acs Nano* **12**, 4719 (2018).

[30] A. Ciarrocchi, D. Unuchek, A. Avsar, K. Watanabe, T. Taniguchi, and A. Kis, *Polarization switching and electrical control of interlayer excitons in two-dimensional van der Waals heterostructures*, *Nature Photonics* **13**, 131 (2019).

[31] E. Torun, H. P. C. Miranda, A. Molina-Sánchez, and L. Wirtz, *Interlayer and intralayer excitons in MoS<sub>2</sub>/WS<sub>2</sub> and MoSe<sub>2</sub>/WSe<sub>2</sub> heterobilayers*, *Phys. Rev. B* **97**, 245427 (2018).

[32] C. Jiang, W. Xu, A. Rasmida, Z. Huang, K. Li, Q. Xiong, and W.-B. Gao, *Microsecond dark-exciton valley polarization memory in two-dimensional heterostructures*, *Nature Communications* **9**, 753 (2018).

[33] A. Srivastava, M. Sidler, A. V. Allain, D. S. Lembke, A. Kis, and A. Imamoğlu, *Optically active quantum dots in monolayer WSe<sub>2</sub>*, *Nature Nanotechnology* **10**, 491 (2015).

[34] P. Tonndorf, R. Schmidt, R. Schneider, J. Kern, M. Buscema, G. A. Steele, A. Castellanos-Gomez, H. S. van der Zant, S. M. de Vasconcellos, and R. Bratschitsch, *Single-photon emission from localized excitons in an atomically thin semiconductor*, *Optica* **2**, 347 (2015).

[35] M. Brotons-Gisbert, A. Branny, S. Kumar, R. Picard, R. Proux, M. Gray, K. S. Burch, K. Watanabe, T. Taniguchi, and B. D. Gerardot, *Coulomb blockade in an atomically thin quantum dot coupled to a tunable fermi reservoir*, *Nature Nanotechnology* **14**, 442 (2019).

[36] P. Nagler, M. V. Ballottin, A. A. Mitioglu, F. Mooshamer, N. Paradiso, C. Strunk, R. Huber, A. Chernikov, P. C. Christianen, C. Schüller, *et al.*, *Giant magnetic splitting inducing near-unity valley polarization in van der Waals heterostructures*, *Nature Communications* **8**, 1551 (2017).

[37] W. Yao, D. Xiao, and Q. Niu, *Valley-dependent optoelectronics from inversion symmetry breaking*, *Physical Review B* **77**, 235406 (2008).

[38] A. Kormányos, G. Burkard, M. Gmitra, J. Fabian, V. Zólyomi, N. D. Drummond, and V. Fal’ko, *k-p theory for two-dimensional transition metal dichalcogenide semiconductors*, *2D Materials* **2**, 022001 (2015).

[39] S. Larentis, H. C. Movva, B. Fallahazad, K. Kim, A. Behroozi, T. Taniguchi, K. Watanabe, S. K. Banerjee, and E. Tutuc, *Large effective mass and interaction-enhanced Zeeman splitting of K-valley electrons in MoSe<sub>2</sub>*, *Physical Review B* **97**, 201407 (2018).

[40] M. Goryca, J. Li, A. Stier, S. Crooker, T. Taniguchi, K. Watanabe, E. Courtade, S. Shree, C. Robert, B. Urbaszek, *et al.*, *Revealing exciton masses and dielectric properties of monolayer semiconductors with high magnetic fields*, *arXiv preprint arXiv:1904.03238* (2019).

[41] G. Wang, E. Palleau, T. Amand, S. Tongay, X. Marie, and B. Urbaszek, *Polarization and time-resolved photoluminescence spectroscopy of excitons in MoSe<sub>2</sub> monolayers*, *Applied Physics Letters* **106**, 112101 (2015).

[42] P. Giannozzi, S. Baroni, N. Bonini, M. Calandra, R. Car, C. Cavazzoni, D. Ceresoli, G. L. Chiarotti, M. Cococcioni, I. Dabo, *et al.*, *Quantum espresso: a modular and open-source software project for quantum simulations of materials*, *Journal of physics: Condensed matter* **21**, 395502 (2009).

[43] D. R. Hamann, *Optimized norm-conserving Vanderbilt pseudopotentials*, *Physical Review B* **88**, 085117 (2013).

[44] M. van Setten, M. Giantomassi, E. Bousquet, M. Verstraete, D. Hamann, X. Gonze, and G.-M. Rignanese, *The PseudoDojo: Training and grading a 85 element optimized norm-conserving pseudopotential table*, *Computer Physics Communications* **226**, 39 (2018).

## ACKNOWLEDGEMENTS

The authors thank J. J. Finley, K. Müller, M. Kremser, and A. Högele for discussions. This work is supported by the EPSRC (grant no. EP/P029892/1 and EP/S000550/1), the ERC (grant no. 725920) and the EU Horizon 2020 research and innovation program under grant agreement no. 820423. AMS acknowledges the Juan de la Cierva (Grant IJCI-2015-25799) program (MINECO, Spain) and the Marie-Curie-COFUND program Nano TRAIN For Growth II (Grant Agreement 713640). The computations were performed on the Tirant III cluster of the Servei d’Informàtica of the University of Valencia (project vlc82). Growth of hBN crystals by K.W. and T.T. was supported by the Elemental Strategy Initiative conducted by the MEXT, Japan and the CREST (JPMJCR15F3). B.D.G. is supported by a Wolfson Merit Award from the Royal Society and a Chair in Emerging Technology from the Royal Academy of Engineering.

## AUTHOR CONTRIBUTIONS

B.D.G. conceived and supervised the project. H.B. fabricated the samples. K.W. and T.T. supplied the hBN crystals. M.B.-G. and H.B. performed the experiments, assisted by C.B. and D.W. M.B.-G. analysed the data, assisted by D.S. and B.D.G. A.M.-S. performed the ab initio calculations. M.B.-G. and B.D.G. cowrote the paper with input from all authors. M.B.-G. and H.B. contributed equally to this work.

## COMPETING INTERESTS

The authors declare no competing interests.

## METHODS

### *ab initio* calculations

The *ab initio* calculations of the electronic structure of the tri-layer MoSe<sub>2</sub>/WSe<sub>2</sub> heterostructure have been performed using Quantum Espresso [42]. We have employed the local density approximation including spin-orbit interaction with

spinorial wave functions, using norm-conserving full relativistic pseudopotentials. The pseudopotentials of Mo and W atoms include semi-core valence electrons and have been generated with **ONCVPSP** [43] and **PSEUDODOJO** [44]. The electronic density converges with an energy cutoff of 80 Ry and a **k**-grid of  $12 \times 12 \times 1$ . We use a slab model with a 10 Å vacuum thickness to avoid interactions between periodic images.